Supplementary Information to *Temperature- and vacancy-concentration-dependence of heat transport in Li_3ClO from multi-method numerical simulations*

Paolo Pegolo
SISSA—Scuola Internazionale Superiore di Studi Avanzati, 34136 Trieste, Italy

Stefano Baroni
SISSA—Scuola Internazionale Superiore di Studi Avanzati, 34136 Trieste, Italy and
CNR—Istituto Officina dei Materiali, SISSA, 34136 Trieste

Federico Grasselli*
COSMO—Laboratory of Computational Science and Modelling, IMX,
École Polytechnique Fédérale de Lausanne, 1015 Lausanne, Switzerland and
SISSA—Scuola Internazionale Superiore di Studi Avanzati, 34136 Trieste, Italy

SUPPLEMENTARY NOTE 1. SLACK MODEL

For a crystal with n atoms per unit cell, whose average atomic mass is $\overline{M}$, thermal conductivity in $\mathrm{Wm^{-1}K^{-1}}$ is estimated as

$$\kappa = \frac{2.43 \cdot 10^{-6}}{1 - 0.514/\gamma + 0.228/\gamma^2} \frac{\overline{M}\Theta_D^3 \delta}{\gamma^2 T n^{2/3}}, \tag{1}$$

where Θ_D is the Debye temperature in K, γ is the Grüneisen parameter, δ is the cubic root of the average atomic volume in Å, and $\overline{M}$ is expressed in atomic mass units. The Debye temperature is computed directly from the Debye model, by evaluating the average sound velocity obtained from the angular average of the sound velocities, which are in turn calculated solving the wave equation for each propagation direction; the other quantities are described in the main text.

SUPPLEMENTARY NOTE 2. BOLTZMANN TRANSPORT EQUATION

Following Barbalinardo *et al.*, [1] let us label the phononic states of a general anisotropic crystal at a finite temperature T by a wave-vector $\boldsymbol{q}$ and a band index s. Phonons populate the available energy levels according to the Bose-Einstein statistic with null chemical potential, *i.e.*

$$n_{\boldsymbol{q}s} = n(\omega_{\boldsymbol{q}s}) = \frac{1}{\mathrm{e}^{\hbar\omega_{\boldsymbol{q}s}/k_\mathrm{B}T} - 1}, \tag{2}$$

with $\omega_{\boldsymbol{q}s}$ the angular frequency of vibration of the normal mode labeled by $(\boldsymbol{q}, s)$. Under the assumption that the phonon population depends on position only through the temperature, in linear response to a small temperature gradient $\nabla_\alpha T$ along direction $\alpha = x, y, z$, the occupation number (2) acquires a contribution proportional to $\nabla_\alpha T$:

$$\tilde{n}_{\boldsymbol{q}s\alpha} = n_{\boldsymbol{q}s} + \lambda_{\boldsymbol{q}s}\nabla_\alpha n_{\boldsymbol{q}s} = n_{\boldsymbol{q}s} + \lambda_{\boldsymbol{q}s}\frac{\partial n_{\boldsymbol{q}s}}{\partial T}\nabla_\alpha T. \tag{3}$$

The quantity $\lambda_{\boldsymbol{q}s}$ is called phonon mean free path. From the $\boldsymbol{q}$-gradient of the phonon frequencies, one obtains the phonon group velocities $v_{\boldsymbol{q}s\alpha} = \frac{\partial\omega_{\boldsymbol{q}s}}{\partial q_\alpha}$; these, together with the phonon energies $\hbar\omega_{\boldsymbol{q}s}$ and the out-of-equilibrium occupation numbers $\tilde{n}_{\boldsymbol{q}s\alpha}$, are used to define the heat current per normal mode as

$$\begin{aligned} j_{\boldsymbol{q}s\alpha'} &= \sum_\alpha \hbar\omega_{\boldsymbol{q}s} v_{\boldsymbol{q}s\alpha}(\tilde{n}_{\boldsymbol{q}s\alpha} - n_{\boldsymbol{q}s}) \\ &\simeq -\sum_\alpha \hbar\omega_{\boldsymbol{q}s} v_{\boldsymbol{q}s\alpha}\frac{\partial n_{\boldsymbol{q}s}}{\partial T}\lambda_{\boldsymbol{q}s}\nabla_\alpha T. \end{aligned} \tag{4}$$

* federico.grasselli@epfl.ch

An expression for the thermal conductivity is retrieved after having introduced the Fourier equation of diffusive conduction, $J_\alpha = -\sum'_\alpha \kappa_{\alpha\alpha'} \nabla_{\alpha'} T$, that relates the macroscopic heat flux $J_\alpha = \sum_{\boldsymbol{q},s} j_{\boldsymbol{q}s\alpha}/(N\Omega)$ to the temperature gradient. Thermal conductivity reads

$$\kappa_{\alpha\alpha'} = \frac{1}{\Omega N} \sum_{\boldsymbol{q},s} \hbar\omega_{\boldsymbol{q}s} \frac{\partial n_{\boldsymbol{q}s}}{\partial T} v_{\boldsymbol{q}s\alpha} \lambda_{\boldsymbol{q}s}. \tag{5}$$

Thus, the computation of κ requires the knowledge of the out-of-equilibrium occupation number. The statistical mechanics of an out-of-equilibrium system can be described by BTE, whose expression is

$$\boldsymbol{v}_{\boldsymbol{q}s} \cdot \nabla T \frac{\partial n_{\boldsymbol{q}s}}{\partial T} = \left.\frac{\partial n_{\boldsymbol{q}s}}{\partial t}\right|_{\text{scatt.}}. \tag{6}$$

The right-hand side is the *scattering term*, whose linearized form contains all the scattering rates relating three-phonons scattering events. The inverse of the matrix of scattering rates is in turn used to compute the phonon mean free paths, which are what is needed to obtain κ. The problem of computing κ is reduced to the calculation and inversion of the scattering rates matrix. This can be demanding, and often requires additional approximations, the simplest of which being the relaxation time approximation (RTA). In RTA, only the diagonal part of the scattering rates matrix is retained: the population of each out-of-equilibrium mode is taken to be interacting with a bath of modes at thermal equilibrium. A way to go beyond this picture is to recast the inversion problem to an iterative equation to be solved self-consistently. [2]

A. Convergence of the IFC3 with the supercell

The Interatomic Force Constant (IFC) matrices are computed via finite differences on a supercell. The second order IFC (IFC2) is calculated inexpensively on a $6 \times 6 \times 6$ supercell. The choice of the supercell for the third order IFC (IFC3) changes substantially the computational cost of the calculations, and requires more care. The IFC3 is computed as a function of the supercell size. This relationship is studied via the so-called "triangle plot". The triangle plot for the IFC3 computed with 2, 4, 6 and 8 unit cells in each dimension is shown in Fig. 1. In the horizontal axis there is the perimeter of the triangle whose vertices are positions of the three atoms involved in each block in the IFC3 matrix, a block being the $3 \times 3 \times 3$ tensor $\frac{\partial^3 U}{\partial \boldsymbol{r}_i \partial \boldsymbol{r}_y \partial \boldsymbol{r}_k}$. In the vertical axis there are the matrix norms of each block. A supercell of size $6 \times 6 \times 6$ is found to be sufficient to have a IFC3 converged up to $\approx 1\%$.

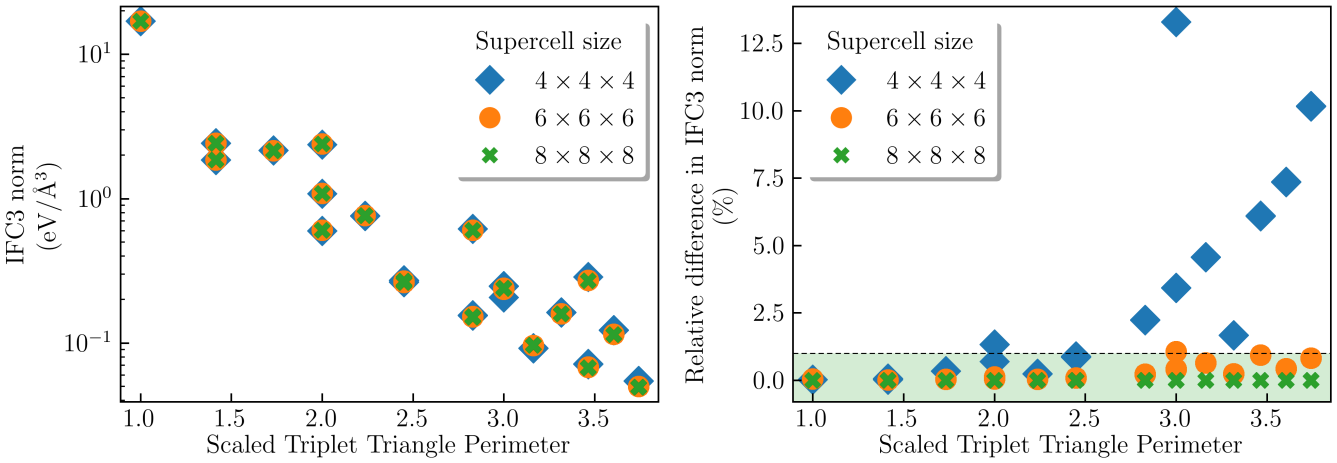

Supplementary Figure 1. Convergence of the IFC3 with respect to the number of supercell size. (*left*) Triangle plots for different supercell sizes. (*right*) Relative difference in the IFC3 norms with respect to the reference one with a $8 \times 8 \times 8$ supercell. The green-shaded area indicates values below 1%.

B. Convergence of the IFC with the number of nearest neighbour shells

The dependence on the number of included nearest neighbour (n.n.) shells of FC3 is studied both via the triangle plot and by directly computing the thermal conductivity tensor, $\boldsymbol{\kappa}$, on a coarse $12 \times 12 \times 12$ $\boldsymbol{q}$-points mesh. The triangle plot for the FC3 computed with $6 \times 6 \times 6$ supercell is shown in the left panel of Fig. 2, while on the right panel there is the relative change in $\boldsymbol{\kappa}$ for a given number of n.n. shells, denoted by $\boldsymbol{\kappa}_{nns}$, with respect to $\boldsymbol{\kappa}_0$, i.e. the thermal conductivity tensor obtained with the highest number of n.n. shells available. Frobenius matrix norms are employed, to take into account the off-diagonal elements as well. A number of n.n. shells equal to 9 is found to be sufficient to have a thermal conductivity tensor converged well below 1%.

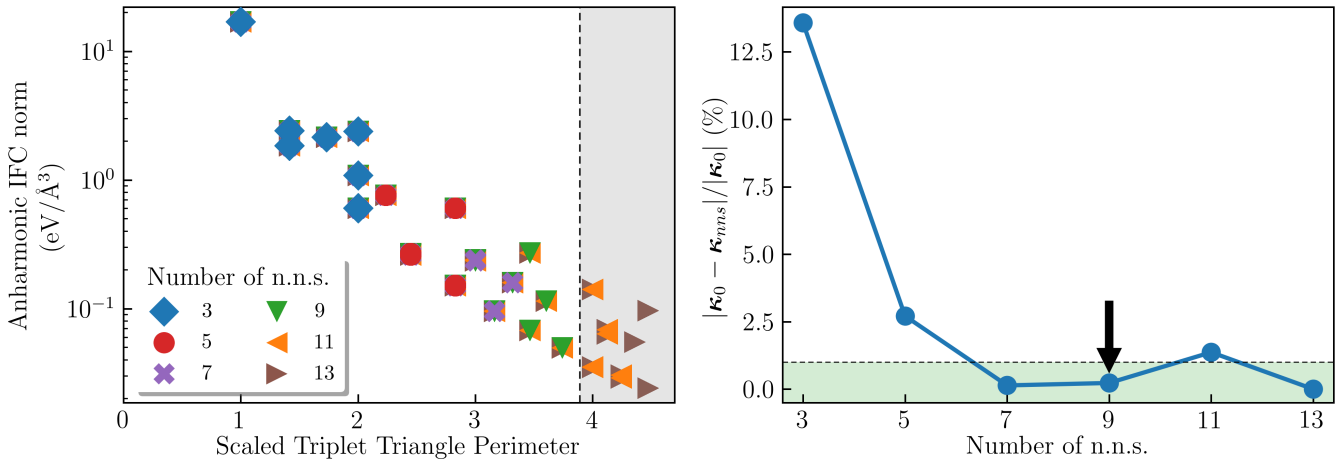

Supplementary Figure 2. Convergence with respect to the number of n.n. shells. (*left*) Triangle plots for diffent values of the number of n.n. shells; (*right*) relative difference (in Frobenius norm sense) in the lattice thermal conductivity from IFC3 computed with different n.n. shells. The green-shaded area indicates values below 1%.

C. Convergence of the thermal conductivity with the number of q-points

The convergence of κ with the number of $N_{\boldsymbol{q}}$ of $\boldsymbol{q}$-points is analysed by computing the thermal conductivity tensor for different reciprocal space meshes for different temperatures. The results are then analysed in terms of the relative change in $\boldsymbol{\kappa}$ for a given $N_{\boldsymbol{q}}$, denoted by $\boldsymbol{\kappa}_{N_{\boldsymbol{q}}}$, with respect to $\boldsymbol{\kappa}_0$, i.e. the thermal conductivity tensor obtained with the highest $N_{\boldsymbol{q}}$ available. Convergence is deemed as satisfactory when the change is consistently lower than 1%. From Fig. 3 one can see that a mesh of $20 \times 20 \times 20$ $\boldsymbol{q}$-points is sufficient to provide converged results.

D. Relaxation time approximation vs. full solution of the BTE

Calculations for selected temperatures are carried out to address the relative importance of the full solution of the linearised BTE with respect to the RTA result. As shown in Fig. 4, it appears that RTA deviates from the full solution of at most $\approx 0.6\%$. Thus, it is employed for the rest of the calculations.

E. Four-phonons contributions

Four-phonons calculations are carried out via the `Fourphonon` code [3], an extension to `ShengBTE`. Since four-phonon calculations are quite expensive, scattering rates and thermal conductivity for three- and four-phonon processes are performed on a coarse mesh of $10 \times 10 \times 10$ $\boldsymbol{q}$-points with IFCs coming from a $4 \times 4 \times 4$ supercell, and with a fourth-order interatomic force constant matrix (IFC4) that includes contributions from the first n.n. shell only. The scale parameter for Gaussian broadening is reduced to 0.1 from the default value of 1.0.

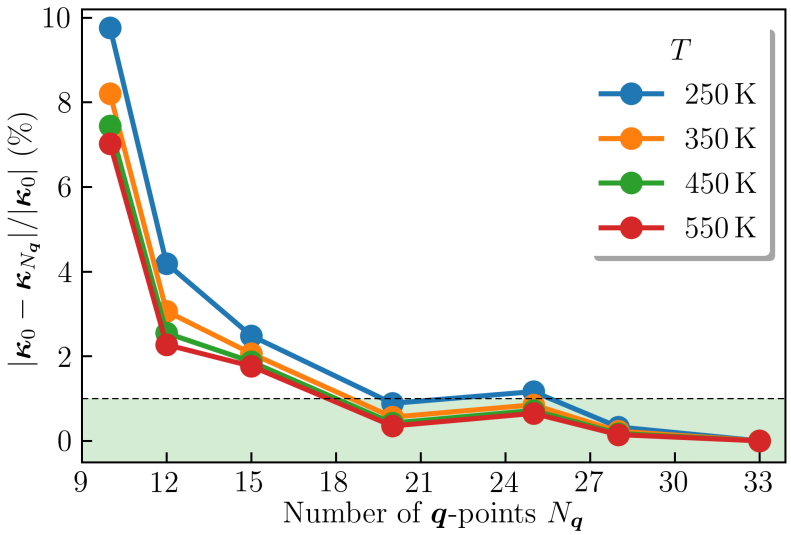

Supplementary Figure 3. Convergence with respect to the number of $\boldsymbol{q}$-points.

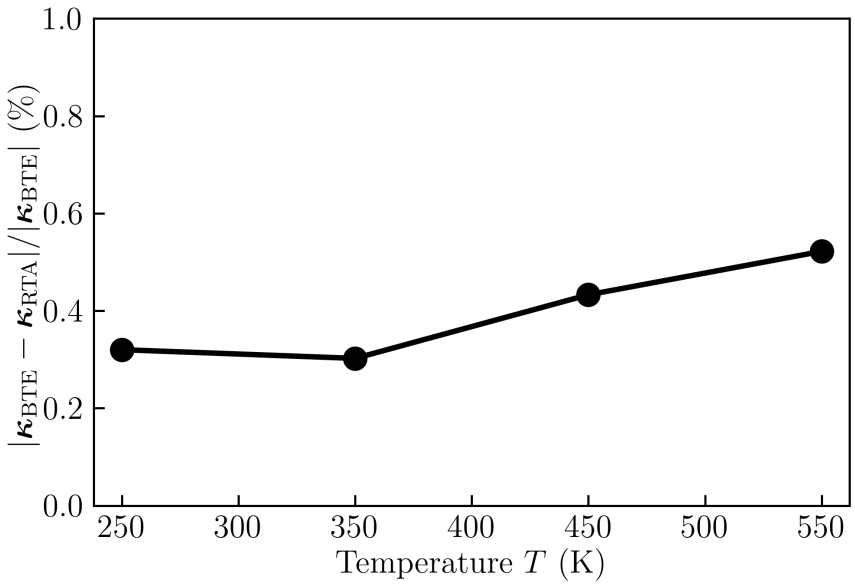

Supplementary Figure 4. Relative difference between the RTA and the full solution to the linearised BTE.

F. Effect of the inclusion of NAC on thermal conductivity

The effect on κ of the inclusion/exclusion of NAC to the dynamical matrix are addressed in Fig. 5. The exclusion of NAC is found to produce a variation of up to 5% to the value of κ in the temperature range of interest.

G. Equipartition vs. Bose-Einstein statistics

In a BTE approach one can choose the statitstics of the phonon occupation numbers. For quantum particles, it is the Bose-Einstein distibution

$$n_{\mathrm{BE}} = \frac{1}{\mathrm{e}^{\hbar\omega/k_{\mathrm{B}}T} - 1}. \tag{7}$$

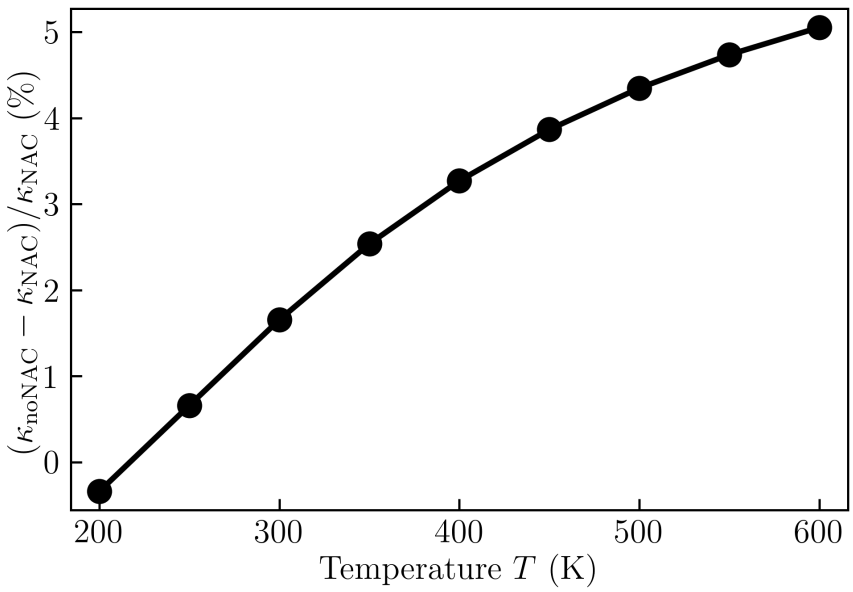

Supplementary Figure 5. Relative difference in thermal conductivity including versus excluding NAC.

MD with classical particles samples the first order expansion of (7) at high temperature

$$n_{\mathrm{BE}} = \frac{k_{\mathrm{B}}T}{\hbar\omega}, \tag{8}$$

i.e. the equipartition law. Since the difference between Eqs. (7) and (8) is always negative at finite T, the thermal conductivity computed with equipartition will be lower than the one computed with Bose-Einstein distribution at the same level of the theory. We have checked how important this difference is for Li_3ClO, by modifying `ShengBTE` to allow occupations according to (8). The results are shown in Fig. 6. As expected being Eq. (8) a high-temperature expansion of Eq. (7), the difference is lower at higher temperatures. This contribution alone, that is around than 5% in most of the temperature range, is not sufficient to explain the difference between the BTE-based and MD-based values of κ.

SUPPLEMENTARY NOTE 3. DATA ANALYSIS

A. Estimation of thermal conductivity from MD simulations

Thermal conductivity is estimated from the power spectrum of the energy flux S_{EE}, after removing its coupling to the mass fluxes, $S_{\mathrm{coupl.}}$, i.e.

$$\kappa(\omega) = \frac{\Omega}{6k_{\mathrm{B}}T^2}\left[S_{EE}(\omega) - S_{\mathrm{coupl.}}(\omega)\right]. \tag{9}$$

Details on the method are found in Refs. [4, 5]. Being the spectrum an even function of ω, its low frequency part needs to be quadratic. Thus, the first portion (up to $\approx 0.1\,\mathrm{THz}$) of the spectrum is fitted to the quadratic function

$$\kappa_{\mathrm{fit}}(\omega)a + b\left(\frac{\omega}{2\pi}\right)^2. \tag{10}$$

An example ($T = 373\,\mathrm{K}$ and $x = 0.005$) of the spectrum of the energy flux decoupled from the mass fluxes is shown in Fig. 7.

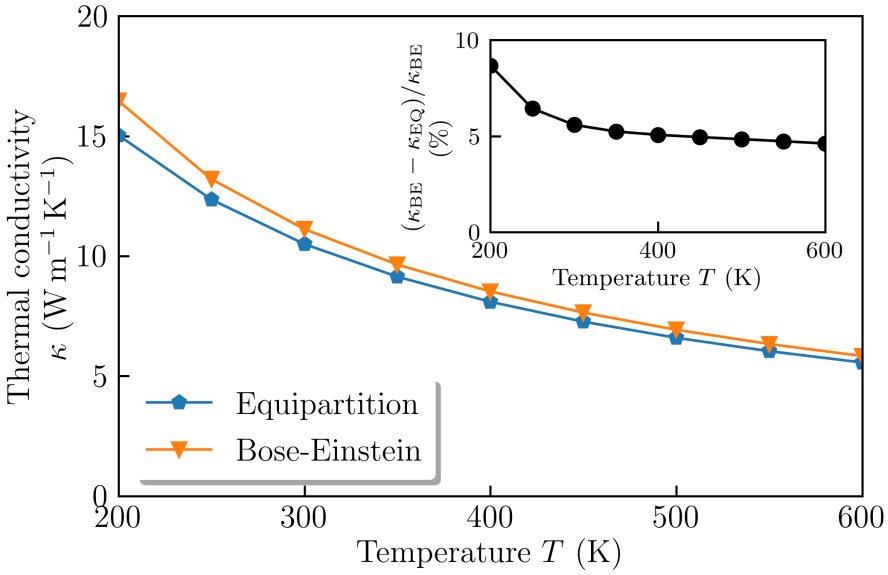

Supplementary Figure 6. Comparison between lattice thermal conductivity computed with Bose-Einstein occupations and with the equipartition law. In the inset, their relative difference is plotted as a function of temperature.

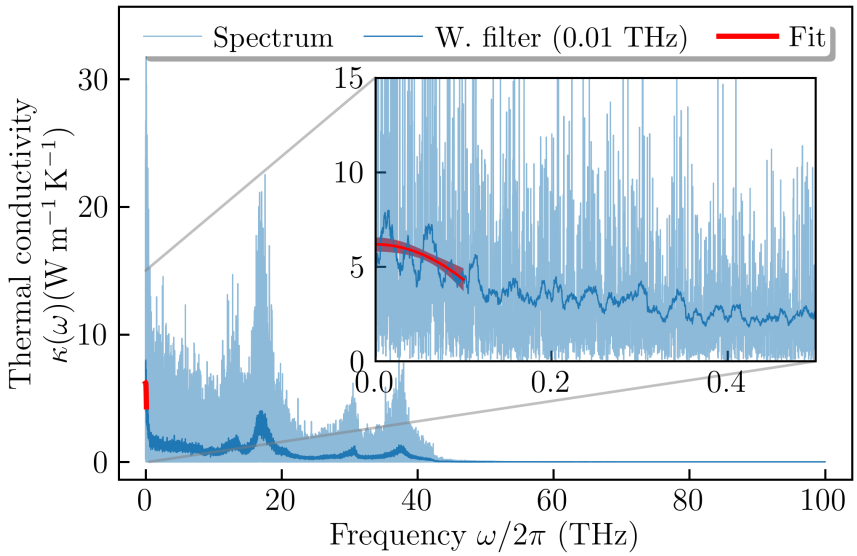

Supplementary Figure 7. Spectrum of the energy flux decoupled from the mass fluxes for the MD simulation at $T = 373\,\mathrm{K}$ and $x = 0.005$. The fit to (10) is done on frequencies up to 0.1 THz.

B. Vacancy-dependent GK thermal conductivity

GK thermal conductivity from FF based MD simulations are fitted for each value of the vacancy concentration x. The fitting function is

$$\kappa_{\mathrm{fit}} = \frac{C_{\mathrm{Euck}}}{T} + C_{\mathrm{AF}}, \tag{11}$$

as derived in the main text. The values of the fitting parameters C_{Euck} and C_{AF}, obtained via standard linear regression of $\log(\kappa)$ versus $\log(1/T)$, are shown in Table I.

Supplementary Table I. Values of the fitting parameters C_{Euck} (in $\mathrm{W\,m^{-1}}$) and C_{AF} (in $\mathrm{W\,m^{-1}\,K^{-1}}$) in Eq. (11).

	$x = 0$	$x = 0.005$	$x = 0.02$	$x = 0.05$	$x = 0.1$
C_{Euck}	2300 ± 120	1560 ± 110	1010 ± 120	590 ± 70	320 ± 90
C_{AF}	0.2 ± 0.3	1.5 ± 0.3	2.1 ± 0.3	2.1 ± 0.2	1.9 ± 0.3

SUPPLEMENTARY NOTE 4. NEURAL NETWORK MODEL

A Deep Potential–Smooth Edition (DeepPot-SE) Neural Network model [6, 7] is trained on a set of AIMD simulations at different temperatures, enriched with additional configurations chosen by the `dpgen` software [8]. The system used for the training of the NN is a $3 \times 3 \times 3$ supercell of Li_3ClO with a LiCl pair removed. The Root Mean Squared Errors (RMSEs) of the trained model are 0.11 ± 0.01 meV/atom and 15 ± 3 meV/Å for the energy and the forces, respectively. The uncertainty on the RMSEs is the standard deviation of the RMSEs of four different models that differ by the choice of the initial random seed.

The locality test [9] is performed to assess the influence of long-range interactions on the NN model, that are not explicitly considered here. For a given atom, the atoms that are within a chosen radius (in PBCs) from it are kept fixed. A random perturbation is applied to the positions of all the other atoms placed outside the sphere. The force acting on the atom at the centre of the sphere are collected for a number of different random perturbations, computed both with the NN model and *ab initio*. The average deviation between the NN and *ab initio* forces, defined as $\sigma_f = \sqrt{\langle |\boldsymbol{F}_{AI} - \boldsymbol{F}_{NN}|^2 \rangle}$, quantifies the dependence of the atom's properties on its neighbours; hence the name of Locality Test. This procedure is carried out for different values of the cutoff and for each atomic species in the system. The results obtained with a $4 \times 4 \times 4$ supercell are shown in Fig. 8. Force deviations are at most compatible with the

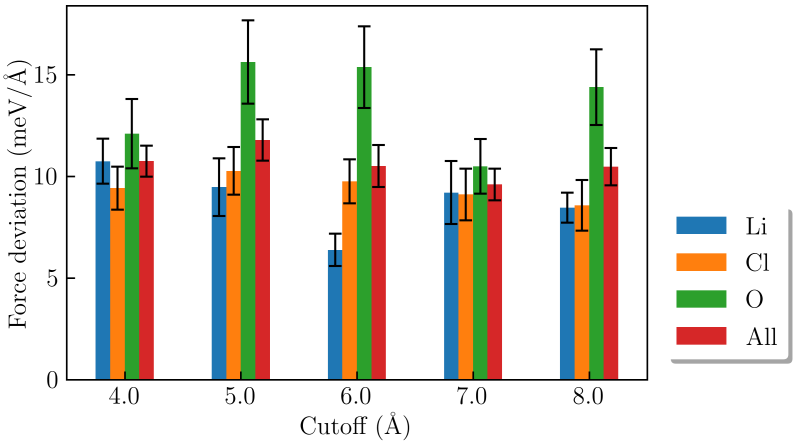

Supplementary Figure 8. Average force deviations for the locality test. The error bars represent the standard deviation of the force deviation sample.

errors on the training, and exhibit a mildly decreasing dependence on the cutoff of the sphere. The error is computed as the standard error on the average of 10 equivalent configurations. This is consistent with the assumption that the local environment is dominant in determining the properties of an atom, and validates the model we employ.

Phonon density of states is computed and compared to the *ab initio* results for different supercells. The results are satisfactory and are shown in Fig. 9.

[1] G. Barbalinardo, Z. Chen, N. W. Lundgren, and D. Donadio, Efficient anharmonic lattice dynamics calculations of thermal transport in crystalline and disordered solids, J. Appl. Phys. **128**, 135104 (2020).
[2] M. Omini and A. Sparavigna, Beyond the isotropic-model approximation in the theory of thermal conductivity, Phys. Rev. B **53**, 9064 (1996).
[3] Z. Han, X. Yang, W. Li, T. Feng, and X. Ruan, FourPhonon: An extension module to ShengBTE for computing four-phonon scattering rates and thermal conductivity (2021), arXiv:2104.04895 [cond-mat.mtrl-sci].

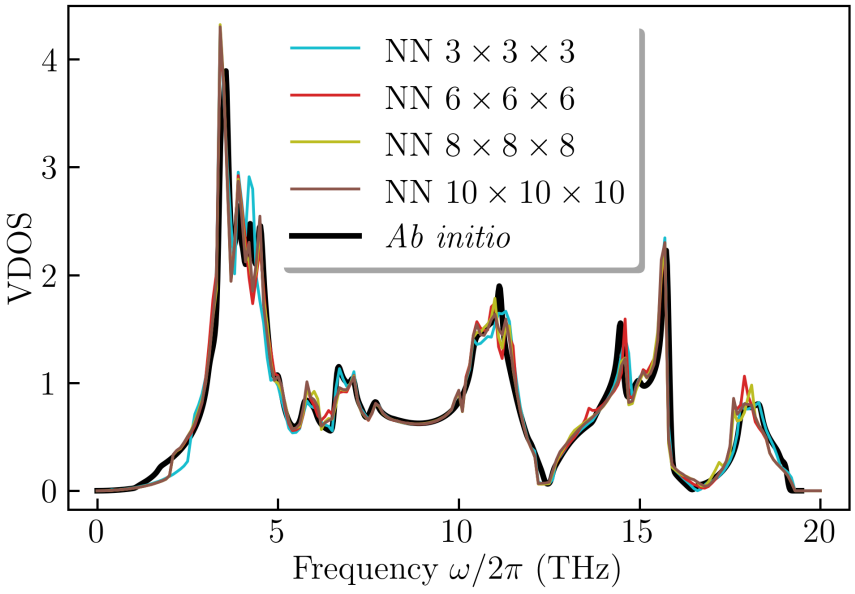

Supplementary Figure 9.

[4] L. Ercole, A. Marcolongo, and S. Baroni, Accurate thermal conductivities from optimally short molecular dynamics simulations, Sci Rep **7**, 1 (2017).
[5] R. Bertossa, F. Grasselli, L. Ercole, and S. Baroni, Theory and numerical simulation of heat transport in multicomponent systems, Phys. Rev. Lett. **122**, 255901 (2019).
[6] J. Han, L. Zhang, R. Car, and W. E, Deep potential: A general representation of a many-body potential energy surface, CiCP **23**, 629 (2018).
[7] L. Zhang, J. Han, H. Wang, W. A. Saidi, R. Car, and E. Weinan, End-to-end symmetry preserving inter-atomic potential energy model for finite and extended systems, Adv. Neur. In. **2018**, 4436 (2018).
[8] Y. Zhang, H. Wang, W. Chen, J. Zeng, L. Zhang, H. Wang, *et al.*, DP-GEN: A concurrent learning platform for the generation of reliable deep learning based potential energy models, Comput. Phys. Commun. **253**, 107206 (2020).
[9] A. P. Bartók, M. C. Payne, R. Kondor, and G. Csányi, Gaussian approximation potentials: The accuracy of quantum mechanics, without the electrons, Phys. Rev. Lett. **104**, 136403 (2010).